External occulter laboratory demonstrator for the forthcoming formation flying coronagraphs

(Article begins on next page)

15 January 2025

External occulter laboratory demonstrator for the forthcoming formation flying coronagraphs

Federico Landini,[1,*] Sébastien Vives,[2] Mélanie Venet,[2] Marco Romoli,[1] Christophe Guillon,[2] and Silvano Fineschi[3]

[1]Dipartimento di Fisica e Astronomia, Sez. di Astronomia—Università di Firenze, Largo Fermi 2, 20125 Firenze, Italy

[2]Laboratoire d'Astrophysique de Marseille, Rue Frédéric Joliot-Curie, Marseille Cedex 13, France

[3]INAF-Osservatorio Astronomico di Torino, Strada Osservatorio 20, 10025 Pino Torinese, Italy

*Corresponding author: flandini@arcetri.astro.it

The design and optimization of the external occulter geometry is one of the most discussed topics among solar coronagraph designers. To improve the performance of future coronagraphs and to stretch their inner fields of view toward the solar limb, the new concept of coronagraphs in formation flight has been introduced in the scientific debate. Solar coronagraphs in formation flight require several mechanical and technological constraints to be met, mainly due to the large dimension of the occulter and to the spacecraft's reciprocal alignment. The occulter edge requires special attention to minimize diffraction while being compatible with the handling and integrating of large delicate space components. Moreover, it is practically impossible to set up a full-scale model for laboratory tests. This article describes the design and laboratory tests on a demonstrator for a coronagraph to be operated in formation flight. The demonstrator is based on the principle of the linear edge, thus the presented results cannot be directly extrapolated to the case of the flying circular occulter. Nevertheless, we are able to confirm the results of other authors investigating on smaller coronagraphs and provide further information on the geometry and tolerances of the optimization system. The described work is one of the results of the ESA STARTIGER program on formation flying coronagraphs ["The STARTIGER's demonstrators: toward a new generation of formation flying solar coronagraphs," in *2010 International Conference on Space Optics (ICSO)* (2010), paper 39].   © 2011 Optical Society of America

OCIS codes: 050.1940, 120.5820, 290.2648.

1. Introduction

The observation of the inner corona (below 1.3 solar radii, being the solar radius, $R_\odot$ equal to 7×10^8 m) is the major challenge the next generation of white-light coronagraphs is going to face. Indeed, the contrast between the inner corona and the solar photosphere (i.e., the visible-light solar disk) is typically ranging between 10^{-6} and 10^{-8}, making coronal observation very difficult. The visible-light corona is an optically thin medium, thus it is observable only out of the solar disk limb by occulting the bright disk source with a suitable stop. On the basis of the occultation concept, we can distinguish between internally and externally occulted coronagraphs. In internally occulted coronagraphs, the occulter is placed on the focal plane of the primary objective, which is hit by the direct solar disk light. These coronagraphs are particularly suited for the observation of the solar corona between 1.1 and $2\,R_\odot$. The observation below $1.1\,R_\odot$ down to the minimum distance achievable from the solar disk limb is prevented by the overwhelming level of stray light, which grows higher and higher by observing closer to the limb. Classical externally occulted coronagraphs are limited, too, in observing the inner corona because of the stray-light level behind the occulter and the very low resolution

due to the presence of the occulter in front of the pupil (vignetting effect). By increasing the distance between the occulter and the pupil, both effects are reduced. The optimal conditions for the observation of the inner corona occur during total solar eclipses; in fact, the large distance between the telescope (on Earth) and the occulter (the Moon) guarantees a very low stray-light level and a minimum vignetting action of the occulter over the pupil. However, eclipses are too rare (only one or two per year) and too short in time (only a few minutes) to allow intensive coronal observations. A way of getting closer to total solar eclipse conditions (thus to observe the inner corona even below $1.1\,R_\odot$ at high resolution) is to enlarge as much as possible the distance between the occulter and the rest of the telescope. The ideal answer to such a highly demanding request is to design, build, and operate two spacecraft (S/C) flying in formation, thus forming a giant solar coronagraph. New challenges are generated by the novelty of the formation flying (FF) concept: by increasing the distance between the S/C, bigger occulters are needed, thus causing difficulties in managing such large optical elements in space. The most critical issue in the design of a white-light solar coronagraph is the reduction of the stray light due to the diffraction and scattering of the solar disk light by the optics. The main source of stray light is the occulting system that must be optimized in order to maximize its efficiency. As experimentally proven by Newkirk and Eddy [1] during a balloon flight, not-optimized occulters fail in fulfilling their goal, since the light diffracted by the occulter edge and scattered by the telescope optics constitutes a contribution of the same order of magnitude of the coronal light. It has been demonstrated by all successful missions (see Section 2 for an historic list of the most successful ones) that an occulter edge shape optimization may lower the level of diffracted light by 2 or 3 orders of magnitude. By combining the FF concept to a suitable optimization of the occulter shape, we satisfy all the requirements in order to maximize the stray-light reduction. In this paper we describe our work on the optimization of large external occulters for future FF coronagraphs, both from logic-theoretical and experimental points of view. Space-borne coronagraph history is characterized by a long debate on the best optimizing shape for the occulter edge, as described in Section 2. The novelty of the FF coronagraph concept (i.e., the coronagraph with the most Moon-like occulter ever conceived, in terms of both occulter–pupil distance and size) does not allow us to completely rely on literature for a choice on the occulter optimization, since all space-borne coronagraphs that are accounted for are within 2 m of length, and all dimensions are scaled more or less accordingly. Therefore, we performed a dedicated study. Although FF solar coronagraphs are a relatively new argument, they have already been discussed by the scientific community, and some missions have been proposed. On this basis, we adopted a practical approach, by focusing

on a particular mission in order to make our considerations directly applicable to a concrete instrument. As a baseline for our investigation, we considered the observational requirements of the PROBA-3/ASPIICS FF coronagraph [2]. Association de Satellites Pour l'Imagerie et l'Interférométrie de la Couronne Solaire (ASPIICS) is a visible-light, externally occulted coronagraph conceived to perform both high spatial resolution imaging and two-dimensional spectrophotometry of the inner corona. It will be implemented on the PROBA-3 mission [European Space Agency (ESA)], which aims at validating developments in space. ASPIICS is distributed on the two PROBA-3 S/C, separated by 150 m. The entrance aperture of the telescope is protected from direct solar disk light by an occulting disk of 1.5 m in diameter. This geometry guarantees an inner field of view of $1.015\,R_\odot$ (i.e., ~14 arcsec overocculation of the solar disk). The optical design of ASPIICS is adapted from the general principles of a classical externally occulted Lyot coronagraph [3]. Section 2 is dedicated to the comparison among pros and cons of the optimization systems that can be found in literature, by considering their performances in stray-light reduction and the issues connected with their possible implementation in the FF mission under study. Sections 3 and 4 are dedicated to the measurements we performed at the Laboratoire d'Astrophysique de Marseille (LAM) to determine occulter optimization performance and manufacturing tolerances. The work described in this paper has been performed in 2010 in the framework of the ESA STARTIGER program supporting the development of future FF solar coronagraphs. The scientific and technical goals of our STARTIGER project are detailed in [4].

2. Literature Heritage and FF Coronagraph Requirements

One of the pioneering papers that faced the occulter optimization issue was by Newkirk and Bohlin [5]; they called the optimization "apodization," while admitting that the phrasing is not entirely appropriate for this kind of optical issue. From their paper: "Diffraction from the external occulting disk is the main source of this stray light. The light diffracted into the objective may be reduced by removing the occulting disk to a great distance, as is the moon at total eclipse, or by 'apodizing' or 'softening' the edge of the disk. (Although 'apodization' commonly refers to the alteration of the Fraunhofer diffraction pattern of an objective lens by means of a radially graded filter, it is here used to describe the modification of the Fresnel diffraction by an opaque disk.) The serrated occulting disk developed by our colleagues at the Naval Research Laboratory is one form of apodization."

Since then, many papers have described optimization systems and analyzed them both from theoretical and experimental points of view. The three most discussed and used systems are toothed disks,

triple disks (in general multiple disks), and a multi-threaded or polished frustum of a right cone (or barrel).

There are five milestone papers on the analysis of the optimization techniques; in chronological order, the main authors are Newkirk [6], Fort [7], Lenskii [8], Koutchmy [9], and Bout [10]. The only system theoretically fully analyzed is the toothed disk [8], while the triple disk and the multithread solution are only qualitatively explained and experimentally tested. In particular, Koutchmy and Bout reported experimental and theoretical (where possible) comparisons among the different optimization systems.

A. Toothed Disk

This method was first proposed by Purcell and Koomen in 1962 [11], and consists of a single disk with a serrated edge. The case has been theoretically analyzed by Lenskii [8], and experimentally tested by Fort *et al.* [7] and Koutchmy [9]. A series of very tiny and sharp teeth was designed to spread diffracted light along the edge of the shadow of the disk itself, in order to escape the pupil. It is the only solution that allows limiting the optimization shape to the plane of the occulter itself, but it is not easily achievable. The main challenge is to manufacture very sharp teeth, which have to be kept very clean. Every single particle that settles on the teeth or in the thin hollow between two successive teeth can scatter light and become a dominant stray-light source; anyway, scattering due to dust settling between two successive teeth can be limited by coupling two disks dephased by half a tooth. Dust is not a major challenge for multiple disks (Subsection 2.B) and optimizing shapes (Subsection 2.C), because they are designed to block light scattered by dust directly exposed to the solar disk. The toothed disk solution has been adopted by several space-borne coronagraphic missions:

- 1963, a NRL team, led by Tousey, obtained the first image of the extended corona with a rocket flight [12];
- 1968–1970, Dollfus flew a coronagraph on a balloon [13];
- 1993–1998, the SPARTAN 201 mission flew an externally occulted coronagraph/spectrometer with a toothed linear occulter to obtain the first UV observation of the extended solar corona [14]; and
- 1995–present, SOHO-Ultraviolet Coronagraph Spectrometer uses the same design concept as the SPARTAN 201 instrument [15,16].

B. Multiple Disks

This system was first proposed and tested by Newkirk and Bohlin in 1963 [6]. A second disk, in the shadow of the first, with respect to the solar disk, blocks the radiation diffracted by the first disk edge and limits the scattering from eventual dust on the first disk; a third disk, in the shadow of the second one, blocks the diffraction produced by the second disk

edge, and so on. Actually, all flown coronagraphs using this solution mounted a three-disk system. Figure 1 describes the concept for a multiple-disk system, by designing just two disks; l is the disk interdistance and z the distance between the external occulter and the entrance pupil of the coronagraph. To add more disks between the two drawn in Fig. 1, it is enough to apply the very same principle. If $r_{2-1} < r_{FOV}$ (and the same inequality holds also for successive disks, if any), then the multiple-disk system has a barrel profile, while, if $r_{2-1} = r_{FOV}$, then the profile is conic. The conic occulter described in Subsection 2.C is designed following this principle. Lenskii [8] performed a theoretical analysis of the stray-light level behind a two-disk system, and extended the result to infer an estimate of the stray-light level behind a three-disk system, but without a proper theoretical analysis. This system has been employed by

- 1965, the balloon-borne Coronascope II of Newkirk and Bohlin [5];
- 1971–1974, the white-light coronagraph in OSO-7 [17];
- 1995–present, LASCO-C3 aboard SOHO [18], that is producing visible-light images of the extended solar corona up to $30\,R_\odot$,
- 2006–present, Cor2 coronagraph and Heliospheric Imager (which uses straight-edge multiple occulters) of the STEREO/SECCHI mission [19]; and
- 2009, HERSCHEL/SCORE [20,21] and HERSCHEL/HeCor [22] coronagraphs, the first two coronagraphs that observed the extended corona in the HeII 30.4 nm line.

Laboratory tests for the GOES-R coronagraph occulter, conducted for a multiple-disk system, demonstrated that, for compact coronagraphs, the barrel profile is preferable to the cone one [23].

C. Cone or Barrel

The multithreaded cone or barrel is the logical extension of the three-disk system; it is basically an improvement of the number of disks, each one in the shadow of the previous, and each one blocking the light diffracted by the previous disk edge. The idea was proposed by Newkirk and Bohlin, but they did not consider this solution very reliable, because of the "inevitable irregularities in the disk" that "throw
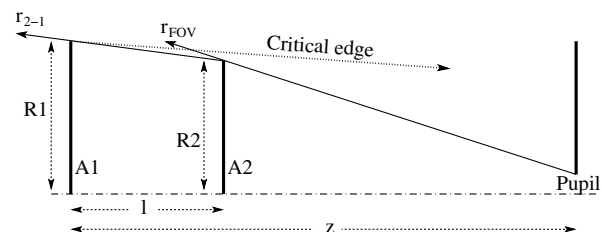

Fig. 1. Concept for the first two disks of a multiple-disk system. The principle is easily repeatable for any other disk that may be inserted between those two. In our case, $z = 150\,\mathrm{m}$, $r_{FOV} = 1.015\,R_\odot$.

spurious radiation into the objective aperture" [6]. This result was overturned by Koutchmy and Belmahdi in experimental tests in 1987 [24]. LASCO-C2 aboard SOHO [18] is using this solution with excellent results. By increasing the number of disks to infinity, we get a polished cone or barrel, which has been compared with the multithread solution only by Bout *et al.* [10]: their result, while confirming Koutchmy and Belmahdi's conclusion, emphasized a substantial equivalence between multithreaded and polished surfaces in stray-light reduction performance, thus suggesting the adoption of polished surfaces, these being easier to manufacture and handle than multithreaded ones.

D. Trade-Off Solutions for the ASPIICS Case

Since the main objective of the coronagraph is to fulfill an observation of the solar corona as close as possible to the limb, *a priori* we tend to exclude optimization systems that increase the inner field of view (FOV). The toothed disk is an example. In fact, while for a multiple-disk system (see Fig. 1) the optimization geometry does not affect the FOV, the teeth of a serrated edge do increase the inner FOV. The toothed disk must be thought of as the baseline sharp disk of 1.5 m diameter plus the thickness of the teeth. By using formula (12) from Lenskii's paper [8], we estimated the diffracted flux on axis behind a toothed disk, normalized to the diffracted flux behind the nominal simple disk for our reference FF coronagraph. Figure 2 shows the result as a function of the number of teeth, for three different tooth peak-to-valley heights (d in Fig. 2). Even in the case of $d = 5$ mm (which fixes the inner FOV at $1.022\,R_\odot$), to obtain a decrease in diffracted light comparable to the 2 or 3 orders of magnitude that are typical for other

kinds of optimization, we should manufacture more than 1×10^5 teeth along the disk circumference. Such a high number corresponds to a peak-to-peak distance of $24\,\mu$m, which is really challenging to machine. Other requirements that have to be matched are the handling and manufacturing for such a huge occulter. Alignment issues must be taken into account, and even pointing stability must be considered. These constraints suggest avoiding long occulting systems, such as the multiple disks, but also a cone would have to be short, i.e., $\sim$10–15 cm at most. We are thus forced to discard a multiple-disk system.

To support this choice, we performed a simple simulation, comparing together the performance of different instruments with a two-disk occulter, as a function of the distance between the disks. Figure 3 (top) shows the result. The y axis of the plot represents the ratio I_2/I_1, where I_2 is the normalized diffracted flux on axis on the entrance pupil plane behind a two-disk system, and I_1 is the same quantity for a single disk. Both values are calculated with the whole solar disk as a source and are given by formulas (8) and (6), respectively, from the Lenskii paper [8].

Three instruments are compared: STEREO-SECCHI/Cor2, HERSCHEL/SCORE, and the 150 m baseline distance FF coronagraph. The x axis is different for each instrument, since they have different dimensions.

It is evident from Fig. 3 (top) that the stray-light reduction due to a two-disk system is improved by increasing the distance between the disks. On the other hand, moving the second disk far from the first one implies an approach to the entrance aperture plane and, thus, a reduction in the instrument collecting area. In the limit of a second disk on the plane
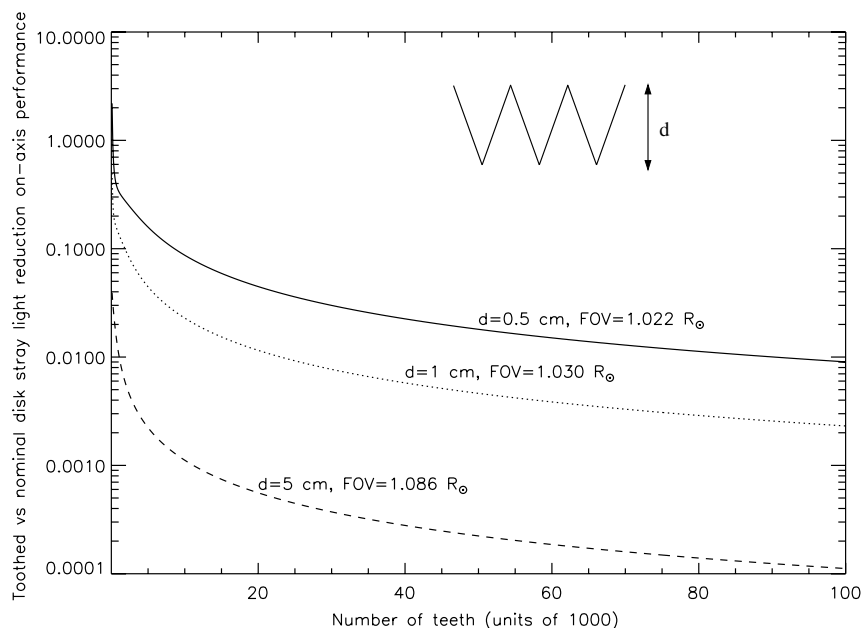

Fig. 2. Ratio between on-axis diffracted light behind a toothed disk and a knife-edge disk, for three different peak-to-valley tooth heights.
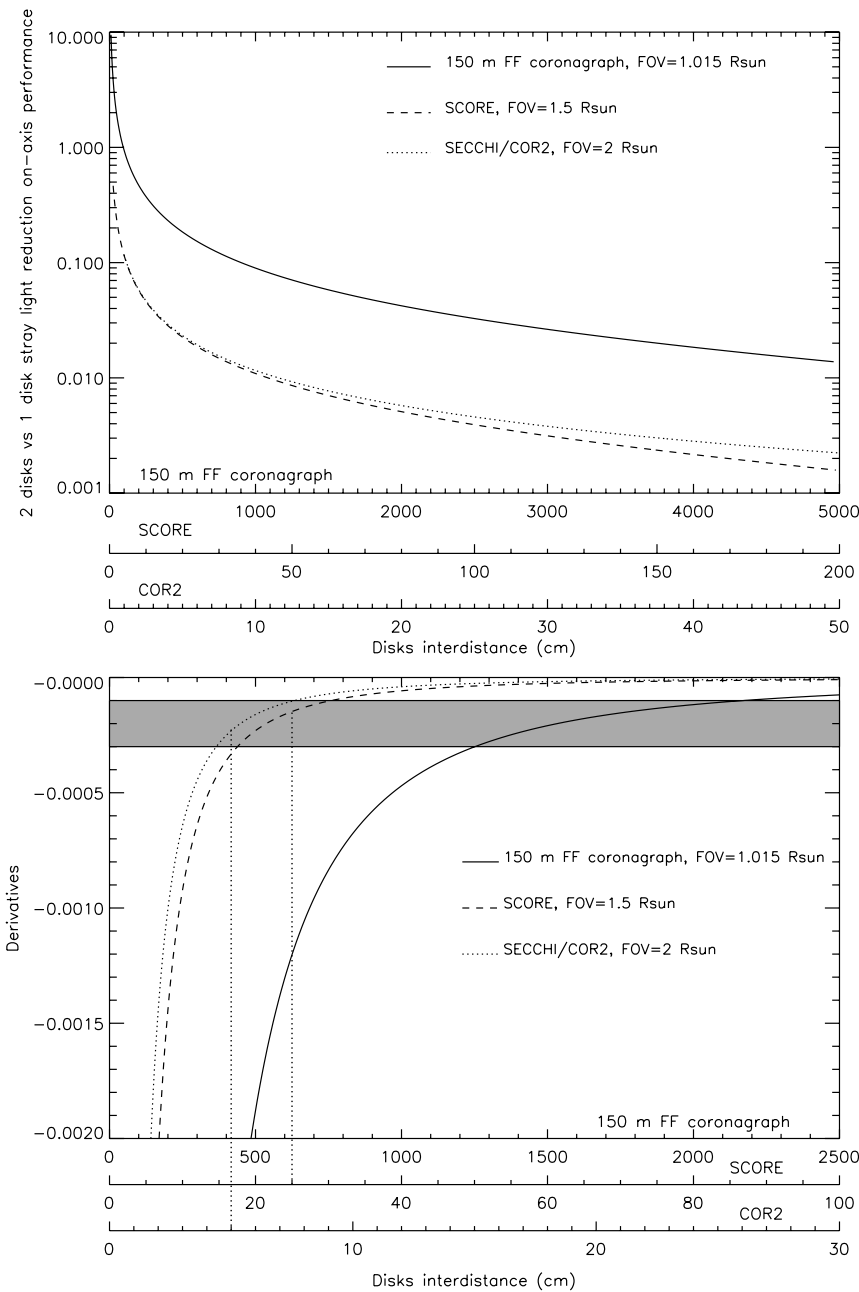
Fig. 3. Comparison among different coronagraphs on stray-light reduction performance (top) as a function of the disk interdistance. The derivative of such performance is shown (bottom) in order to define a procedure to fix the more advantageous trade-off disk interdistance (see text).

of the entrance aperture, we would get a removal of the stray light, as well as of the coronal signal. A trade-off must be found.

A comparison between the diffraction level and a predefined threshold may not be an appropriate method, since the instruments have different FOVs: in general, at fixed geometry, the observation at higher minimum FOV induces a lower level of stray light behind the disks, as confirmed by Fig. 3 (top). This is due to a fainter source (obtained by observing farther from the solar disk limb) diffracted by the occulter edge.

A reasonable way of judging the effectiveness of a second disk is to compute the derivative of the ratio I_2/I_1, which is shown in Fig. 3 (bottom).

Neither the Cor2 nor the SCORE disk interdistance was chosen by using these simulations; nevertheless, this plot is evidence to support the goodness of those choices. The interdistance of two disks is 25 cm for SCORE and 5 cm for Cor2. Both disk interdistances correspond to derivative values in the range $(-3 \times 10^{-4} \div 10^{-4})$, which can be seen as the range where the ratio slope starts smoothing, i.e., the effectiveness of a second disk starts to be less

advantageous. Moving disks farther beyond that interdistance would not bring the same improvement in stray-light reduction as for shorter interdistances. If we imagine applying the same principle to the coronagraph in FF, we would need an impracticable separation between the two disks of at least 12.5 m.

As a rule of thumb, the conic occulter should also keep the same dimensions as the multiple-disk system, since they share the same design principle (see Fig. 1). But a conic occulter has never been simulated, so the previous statement cannot be confirmed. Moreover, if we consider a conic surface (or barrel) and not a multithread with a conic profile (or barrel), the material, the machining, and the surface finish can all affect the performance: laboratory tests are needed to assess these unexplored aspects.

Since polished or electro-eroded cones (or barrels) are more easily machined and less expensive than multithreaded ones while offering comparable performance [10], we decided to concentrate on the former ones, leaving to future analyses a comprehensive evaluation.

Figure 4 shows that, if we draw a barrel following the same principle that we use for a multiple-disk system (see Fig. 1), then, over a length of 15 cm, we get $R_c - R_b \sim 4\,\mu$m, which means that the cone or barrel has the same shape within the manufacturing tolerances. However, it is possible to investigate compact barrels with different design principles (see Subsection 4.D).

3. Laboratory Setup

A test setup has been assembled at the LAM, inside a Class 100 clean room, using the solar simulator implemented for the tests of the LASCO-C2 coronagraph [10]. Since it is practically impossible to realize a full-scale model of the 150 m baseline FF coronagraph, we designed a setup that is able to measure the stray light behind a section of the whole occulter. The section of such a large occulter (1.5 m diameter) can be well approximated by a small straight-edge piece.

We therefore measured the diffraction pattern behind a linear occulter and not behind a disk; thus, it is not possible to directly extrapolate our present results to the actual coronagraph. Nevertheless, it is possible to perform a relative analysis, by comparing stray-light reduction performance of linear occulters.
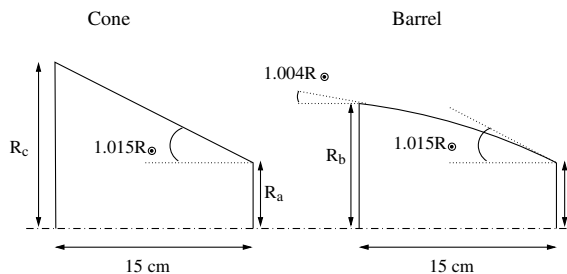
Fig. 4. Cone geometry compared to barrel: if we follow the same principle in designing the two optimizations (see Figure 1), given the flight geometry, differences are negligible ($R_c - R_b \sim 4\,\mu$m).
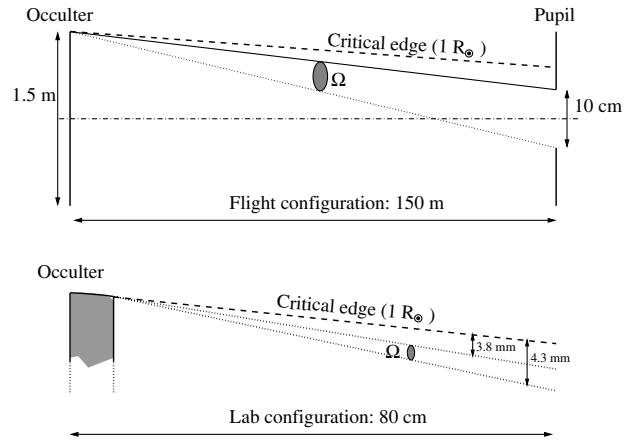
Fig. 5. Comparison between flight (up) and laboratory (down) configurations. The critical edge is defined by the ray coming from the solar limb.

The light diffracted from a knife edge, being easily computable even for an extended source (see Subsection 4.A), is the reference for all the sets of measurements.

It is reasonable to measure the stray-light pattern behind the occulter in the same solid angle defined by the space real-model geometry. Figure 5 shows a comparison between laboratory and flight geometries. The stray light we are interested in is the portion of all the light scattered by the occulter edge that is collected by the telescope entrance pupil. So we measured the stray-light pattern in the solid angle Ω subtended by the pupil as seen by the occulter edge (Fig. 5, top). This created some challenging issues in the laboratory configuration, since we had to measure the stray-light pattern very near to the solar disk critical edge (Fig. 5, bottom), which is defined by the ray coming from the solar limb, grazing the occulter edge.

A sketch of the measurement setup is represented in Fig. 6. A complete overview of the setup concept is shown in Fig. 6(a): the source is a collimator that simulates the angular dimension of the real solar disk. Light from the source enters the Class 100 clean room through an aperture. In the clean room, the stray-light measurement setup is assembled.
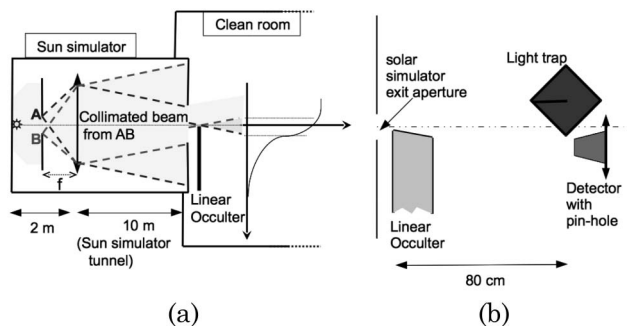
Fig. 6. Not to scale sketch of the measurement setup. (a) Overview of the complete setup, divided into two separated rooms, communicating only by the exit aperture of the source. (b) Particular of the optics setup for stray-light measurement behind the occulter.
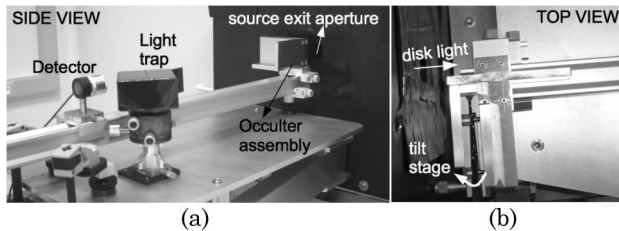
Fig. 7. (a) Overview of the whole optical setup. (b) Particular of the optical setup showing the occulter assembly, as seen from the top of the optical bench: the tilt of the tilting platform is emphasized by an arched white arrow.

The detector is a photodiode mounted on a translation stage. In front of the photodiode is mounted a baffle, accommodating a 0.45 mm pinhole, to allow a high spatial resolution sampling. A light trap is placed very near to the detector to prevent direct "solar" disk light from illuminating the room. Stray-light measurements are performed behind the linear occulter along a direction perpendicular to the occulter edge. All measurements are relative to the source unobstructed flux (i.e., without the occulter mounted). A complete overview of the optical setup is shown in Fig. 7(a).

To achieve the conic angle of the optimized linear occulter, we used a metal plate mounted on a precision steel tilting platform. This also allowed us to define the tolerance we can afford in manufacturing the conic optimization shape, by repeating the stray-light measurement behind the occulter for several conic angles (i.e., several tilting platform tilts, as described in Subsection 4.C.4). Figure 7(b) shows the tilting platform together with the whole linear occulter assembly, as seen from the top of the optical bench.

4. Measurements

A. Knife Edge: Theory

The diffraction pattern behind a linear occulter is relatively easy to compute, even considering an extended source like the solar disk.

Using the Huygens–Fresnel theory [25], the normalized diffracted light intensity pattern behind a perfect and infinite knife edge for a point source at infinity is given by

$$I(x,\lambda) = \frac{1}{2}\left\{\left[\frac{1}{2}+C(\alpha)\right]^2 + \left[\frac{1}{2}+S(\alpha)\right]^2\right\}, \quad (1)$$

where λ is the wavelength, x is the coordinate on the image plane along the direction perpendicular to the occulter edge, $\alpha = x\sqrt{2/(\lambda L)}$, with L distance between the occulter and the image plane, i is the imaginary unit, and $C(\alpha), S(\alpha)$ are the Fresnel integrals. By integrating Eq. (1) over the solar disk, after some brief analytical calculations, we get

$$I_S(x,\lambda) = \frac{1}{\pi R_\odot^2}\int_{-R_\odot+x}^{R_\odot+x} B(x_S)\mathrm{d}x_S\left\{\left(\frac{1}{2}+C(\alpha_S)\right)^2 + \left(\frac{1}{2}+S(\alpha_S)\right)^2\right\}, \quad (2)$$

where x_S is the coordinate along the solar disk radius, $\alpha_S = \sqrt{2/(\lambda L)}(x-x_S)$, and $B(x_S) = \sqrt{R_\odot^2 - (x_S-x)^2}$. Figure 8 compares the diffraction given by Eqs. (1) and (2) at a fixed wavelength of 500 nm. The 0 of the x axis corresponds to the point where the line defined by the center of the Sun and
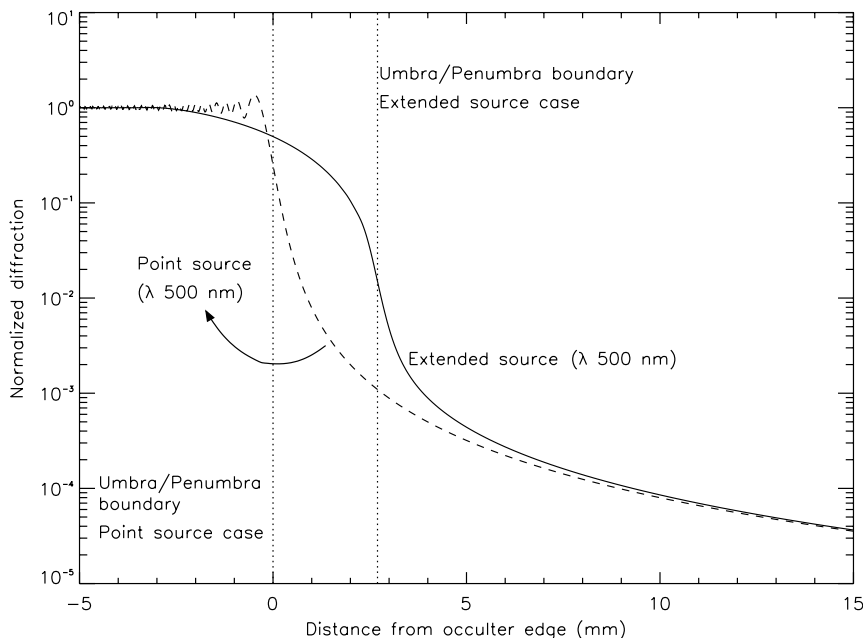

Fig. 8. Theoretical diffraction at a fixed wavelength (500 nm) behind a knife edge in case of point source at infinity (dashed curve) and extended source (solid curve).

the center of the occulter edge intersects the image plane. It can be interesting to note that we can easily recognize the penumbra and umbra (i.e., diffraction) zones in the curves. The inflection point on the descent defines the border between umbra and penumbra; in fact, in correspondence of that point, the light abruptly changes its decreasing slope.

Actually, for rigor's sake, we must consider that the photodiode integrates the signal on its wavelength range of responsivity, so, to get a proper simulated signal, we shall average over the wavelength, including the wavelength dependence of each optical element that the radiation goes through. We call $T(\lambda) = R(\lambda) \cdot W(\lambda) \cdot \Gamma(\lambda)$ the total efficiency of the optical system as a function of the wavelength. $R(\lambda)$ is the responsivity of the photodiode, $\Gamma(\lambda)$ is the spectral distribution emitted by the halogen lamp that is the source of the solar simulator, and $W(\lambda)$ is the transmittance of the two Wratten 80 A filters used to change the color temperature of the radiation; we consider the transmission of the collimator as a constant over the wavelength. With these assumptions, Eq. (2) becomes

$$I_S(x) = \frac{1}{\pi R_\odot^2} \frac{1}{\int_{\lambda_i}^{\lambda_f} T(\lambda) \mathrm{d}\lambda} \int_{\lambda_i}^{\lambda_f} \int_{-R_\odot+x}^{R_\odot+x} \left\{ \left[\frac{1}{2} + C(\alpha_S(x_S, x, \lambda)) \right]^2 \right.$$
$$\left. + \left[\frac{1}{2} + S(\alpha_S(x_S, x, \lambda)) \right]^2 \right\} T(\lambda) B(x_S) \mathrm{d}x_S \mathrm{d}\lambda. \quad (3)$$

In the simulation we included the nominal curves for the spectral distribution of the lamp, the transmittance of the Wratten 80 A filters, and the responsivity of the photodiode. Taking into account

the uncertainty provided by the manufacturers, we computed a tolerance of $\pm 20\%$ on simulated data. Figure 9 shows the simulation as a range that takes into account the uncertainty.

B. Knife Edge: Measurement

With the setup described in Section 3, we performed a measurement to check the agreement of the measured diffraction pattern behind the knife edge and the signal foreseen by Eq. (3). Figure 9 shows a very good agreement between theory and measurements, thus confirming the reliability of the experimental setup. In particular, we may notice that, in the penumbra range, the simulation path is perfectly symmetrical with respect to data values, while, in the diffraction range, the simulation slightly underestimates the measures. This effect can be interpreted as a contribution given by some stray-light sources still present in the measurement environment: since data still fit the uncertainty-weighted simulation range, we assume this stray-light contribution to be negligible. The measurement of diffracted light behind a knife edge is a major step in our analysis, since it validates the experimental setup and allow us to use the nominal values of the simulation as a reference for all the successive tests.

C. Cone

With the setup described in Section 3, various conic configurations have been applied to the linear occulter. Even though we dealt with a tilted metal plate, we interpret it as a portion of a much bigger flight occulter; thus, in the following, we will always refer to it as a cone. To understand how longitudinal
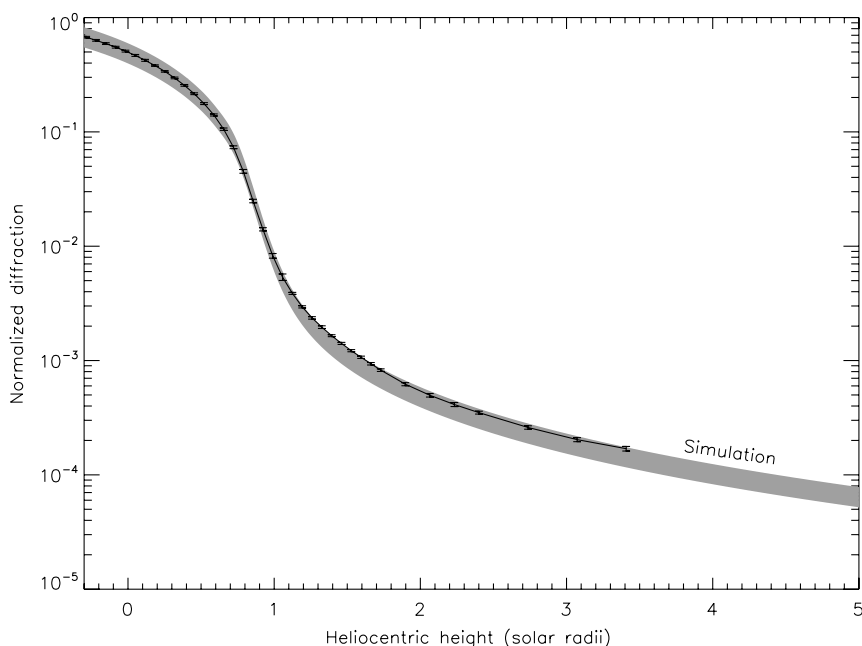

Fig. 9. Measurements of diffracted light behind a knife-edge occulter (black curve) compared to the simulation (gray pattern: the uncertainties provided by the manufacturers are included). A mean behavior of the simulation will be shown as a reference in all successive plots.

dimension, materials, surface polishing, scratches, and assembly errors affect the stray-light reduction performance of the optimized occulter, we performed several indicative tests, for each of which a different occulter was designed and manufactured.

A1: aluminum, 10 cm long, surface roughness $\sigma = 0.4\,\mu$m, which is compared with all the other cone models.

A2: aluminum, 15 cm long, $\sigma = 0.4\,\mu$m, to investigate how length affects performance.

I1: Invar, 10 cm long, $\sigma = 0.4\,\mu$m, to compare different materials' performance.

A3: aluminum, 10 cm long, $\sigma = 0.4\,\mu$m, separated in two equal parts, A3G and A3D, to test if there are differences in stray-light reduction performance between an occulter manufactured as one piece and an assembled one.

A4: aluminum, 10 cm long, $\sigma = 6.4\,\mu$m, to check whether a different surface finishing affects occulter performance.

A5: a spare of A1, surface scratched at a depth of $20\,\mu$m, to check at which level scratches start to affect occulter performance.

A6: a spare of A1, surface scratched at a depth of $200\,\mu$m, with the same objective as A5.

Laboratory tests reveal that there is no difference in stray-light reduction among A1, I1, and A4. It is not necessary to show such measurements, since the curves are overlapped within the errors. This suggests that neither cone material nor its mechanical surface finishing affect stray-light reduction performance (see also Subsection 4.C.3). In any case, Fig. 10 reveals that the conic optimization does indeed improve stray-light performances with respect to the simple knife edge.

1. Length

From Fig. 10 we may also conclude that an increase in the occulter longitudinal length (i.e., along the optical axis) improves the performance, as is evident from the comparison between A1 and A2. This was somehow expected, as the ideal conic optimization for the occulting disk should be much longer than 15 cm, according to the design principle exposed in Subsection 2.B and to the comment in Subsection 2.D.

2. Bad Assembly

If the flight occulter will be made of smaller components, assembly errors may occur. To infer how much assembly errors may affect the optimization performance, tests were made by bad assembly of A3G and A3D on purpose. We define "radial" assembly error as a misalignment along the ideal radius of the flight occulter, i.e., perpendicular to the conic surface. We define "longitudinal" assembly error as a misalignment perpendicular to the previous one, i.e., parallel to the conic surface. We applied a longitudinal misalignment of 1.5 mm and a radial misalignment of 0.5 mm. Figure 11 shows that if the assembly error is radial, we completely jeopardize the optimization effect, while if it is longitudinal, we have no significant impact on the stray-light reduction performance.

3. Scratches

Figure 12 describes how scratches influence the performance of the optimized occulter. Scratches were realized by means of a drill, with a depth of $20\,\mu$m on A5 and $200\,\mu$m on A6. This result allows us to establish that scratches at least $20\,\mu$m deep do not
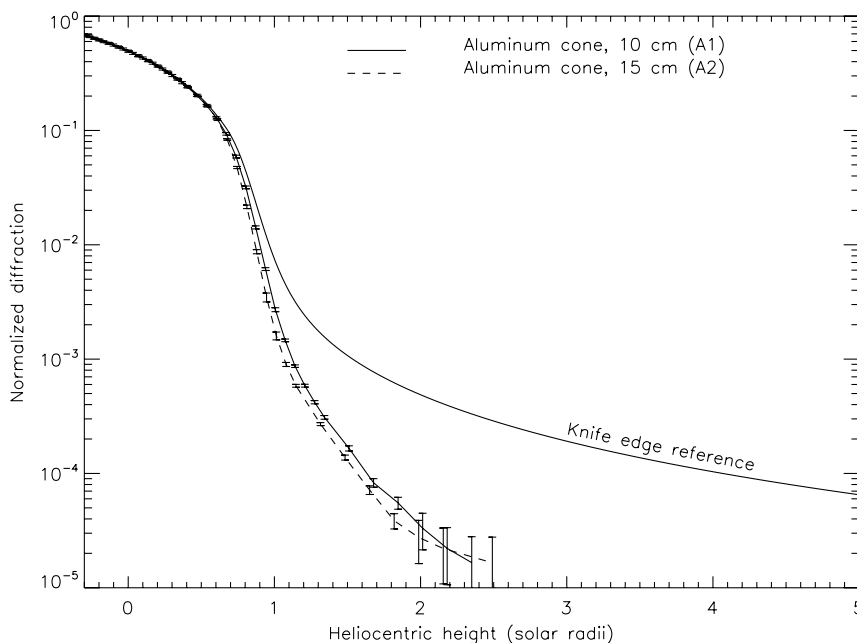

Fig. 10. Comparison among A1, A2, and the knife-edge reference (see Fig. 9 caption).
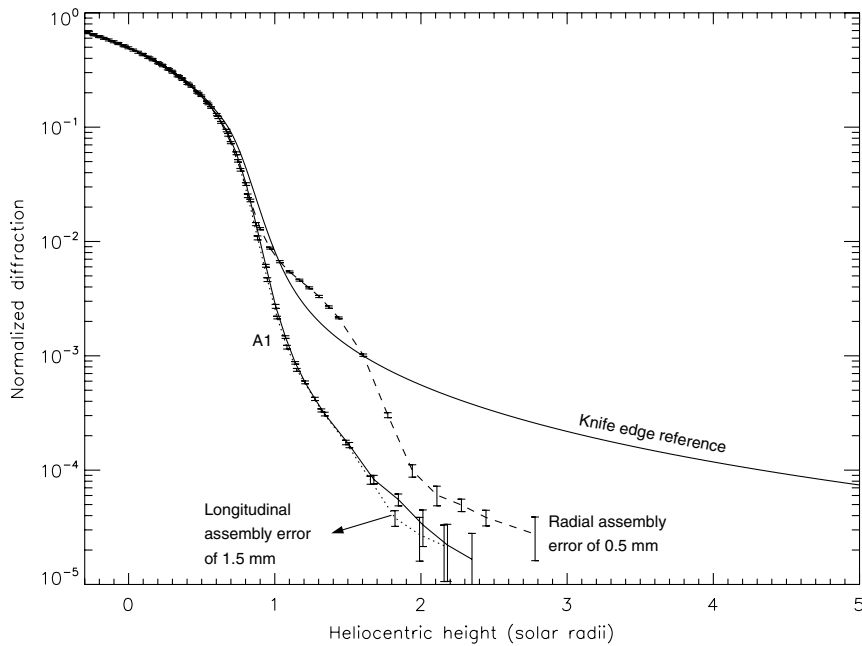
Fig. 11. In the case of an assembled cone, radial assembly errors deeply affect optimization performance, while longitudinal assembly errors are practically ineffective.

affect stray-light reduction performance of the optimized occulter surface.

4. Cone Angle

Figure 13 shows how the cone angle influences stray-light reduction performance. Strangely enough, it seems that we can manufacture a cone with an angle increase within 2 arcmin from the nominal 34.05 arcmin (defined according to the nominal FOV of the instrument and to the principle of Fig. 1). To simulate different cone angles with our linear

optimizing plate, we performed several measures by changing the angle defined by the tilting platform on which the linear occulter was mounted [see Fig. 7(b)]. We obtained a deviation from the nominal behavior (case of A1 in Fig. 10), only beyond 36 arcmin. This result may sound queer since a pure geometric discussion would lead to the conclusion that, by changing the cone angle from the nominal value, we would completely compromise the drawing principle, and thus the performance that it may provide. It may be an interesting result also for types
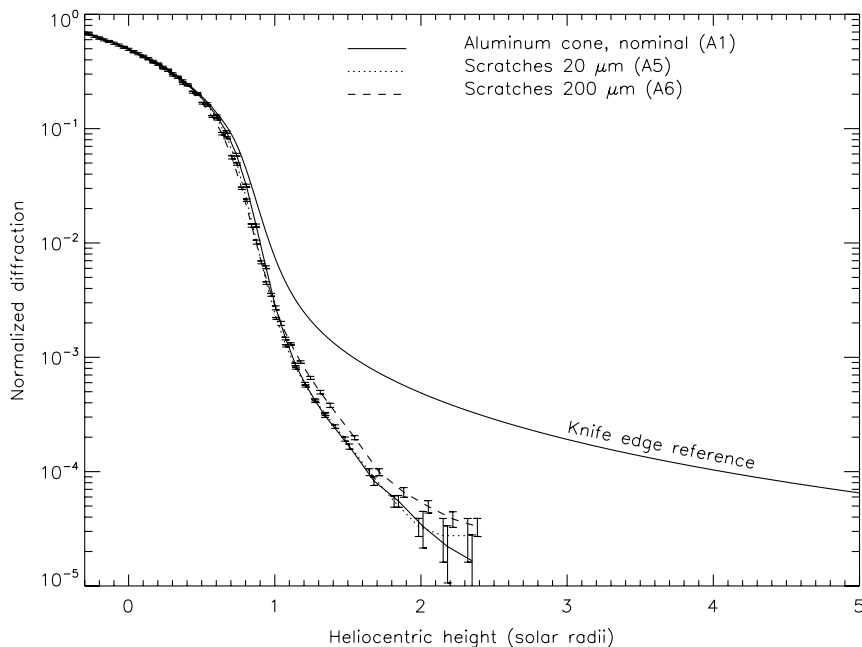

Fig. 12. Comparison among two types of A1s with scratched surfaces and A1 (with no scratches).
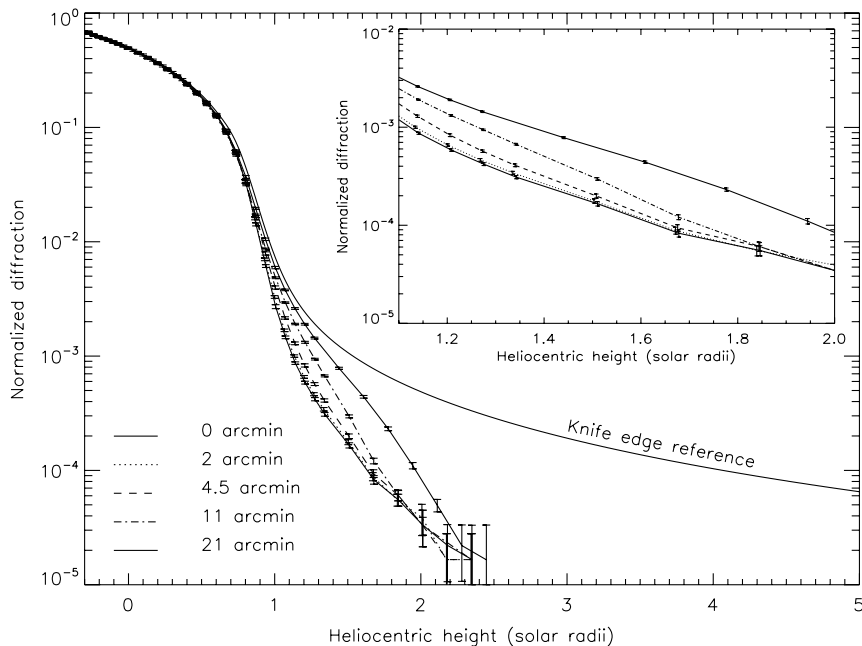
Fig. 13. Analysis on the tolerance we can afford in manufacturing the cone angle. The box enhances a subrange of the main plot between 1.1 and $2\,R_\odot$.

of coronagraphs other than FF ones, for example, standard coronagraphs that are designed to observe the solar corona at different distances from the Sun, such as those aboard Solar Probe [26] or Solar Orbiter [27]. A unique geometry could guarantee good stray-light reduction performance at different distances from the Sun (i.e., at different instrumental FOV).

D. Toroidal Occulters

In Subsection 2.D, we noticed that, due to the geometry of FF coronagraphs, when designing a barrel with the principle of Fig. 1, we cannot deviate appreciably from a cone. In any case, we can change arbitrarily
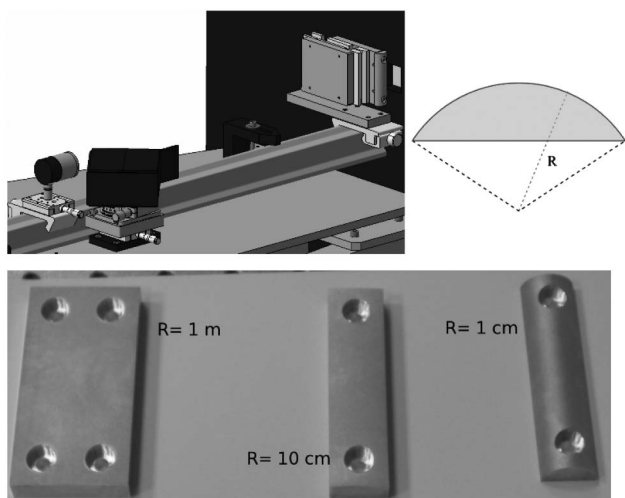

Fig. 14. Clockwise, from the top left: 3D CAD model showing the 1 cm radius occulter mounted in the setup; sketch showing a section of the toroidal occulter, in order to define the curvature radius R; picture of the three manufactured toroidal occulters.

the barrel designing principle, and compare its performance with the conic occulter. We designed three different linear occulters with a cylinderlike geometry, that, if extended on the FF external occulter profile, gives rise to toroidal shapes. These occulters differ in the radius of curvature. To investigate the widest possible field of geometries, we chose to adopt 1 cm, 10 cm, and 1 m as radii. Figure 14 shows the three manufactured occulters, together with a three-dimensional (3D) CAD model of the 1 cm occulter mounted in the setup and a sketch showing the curvature radius definition. All the three toroidal occulters were made of aluminum by electro-erosion. Figure 15 shows the performance of the three toroidal occulters compared with A1. The 1 cm toroidal occulter is the worst of the three, and performances increase by flattening the surface. The 100 cm radius occulter, which is in fact almost flat, has a behavior comparable with the conic occulter. On the other hand, sensitivity to occulter tilt is negligible for the 1 cm toroid, and is the same as A1 for the 100 cm one.

5. Conclusions

In the framework of the ESA STARTIGER program for coronagraphs in FF, a trade-off study was performed for the optimization of the 1.5 m diameter external occulter of a 150 m baseline distance FF coronagraph (such as ASPIICS). The analysis was both qualitative (based upon theoretical and laboratory descriptions in literature) and quantitative. In fact, several sets of measurements were performed at the LAM (France), with a setup mounted in a Class 100 clean room and using a solar simulator source. Since it is impossible to replicate in the laboratory the flight configuration, the measurements were performed on linear occulters, thought of as small
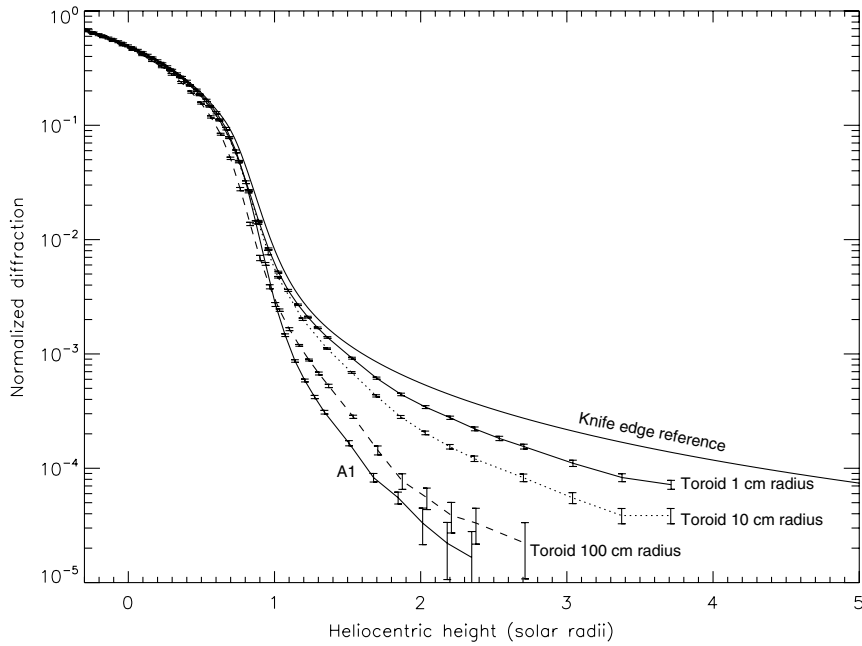
Fig. 15. Comparison among the three toroidal occulters, A1, and the theoretical knife-edge curve.

portions of the big circular occulter. Therefore, it is not possible to directly extrapolate our present results to the actual coronagraph, even though the obtained results provide important information on the best type of optimization and on the manufacturing tolerances. An improvement of the described work is currently ongoing, to confirm that scaled models of the big occulter give the same information as the linear occulters. The results of the current project will be the subject of a forthcoming publication.

All our results are relative to the unobstructed flux and to the knife-edge stray-light reduction performance.

Figure 16 effectively summarizes the main result we obtained, by representing the ratios of each optimized solution performance and the knife-edge reference. Within the limitations due to the use of linear occulters in place of actual disks, our analysis confirms that an optimization improves the stray-light reduction performance of a knife edge. If we think of the straight edge as a portion of a large circular occulter, we may infer that an optimized shape improves the simple disk performance, even in the case of a huge occulter and for very compact shapes along the optical axis.
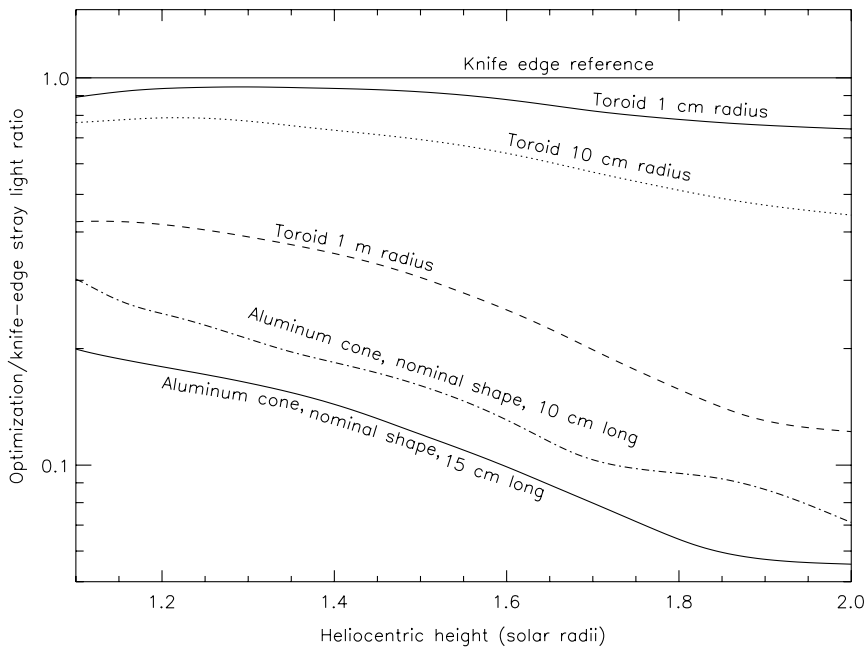

Fig. 16. Ratios among optimized solutions' performance and knife-edge reference.

A conic shape is the best solution, and performance improves by increasing the length of the cone axis. The optimization is not deeply affected by the choice of the material and the surface finishing: even scratches (up to $20\,\mu$m of depth) do not change the optimized occulter performance. Our analysis shows also that such a system is relatively insensitive to tilt (within 2 arcmin) and scratches (at least $20\,\mu$m deep) on the conic surface. We tested also some toroidal apodizations, which are less efficient than the conic ones.

References

1. G. Newkirk, Jr. and J. A. Eddy, "A coronograph above the atmosphere," Sky & Telescope **24**, 77–81 (1962).
2. P. Lamy, L. Damé, S. Vives, and A. Zhukov, "ASPIICS: a giant coronagraph for the ESA/PROBA-3 Formation Flying Mission," Proc. SPIE **7731**, 773118 (2010).
3. J. W. Evans, "Photometer for measurement of sky brightness near the Sun," J. Opt. Soc. Am. **38**, 1083 (1948).
4. S. Vives, L. Damé, P. Lamy, A. Antonopoulos, G. Burton, G. Capobianco, G. Crescenzio, V. Da Deppo, M. Ellouzi, S. Fineschi, J. Garcia, C. Guillon, F. Landini, A. Marshall, A. Mazzoli, P. Rochus, T. Soilly, F. Stathopoulos, C. Tsiganos, K. Tsinganos, and N. Waltham, "The STARTIGER's demonstrators: toward a new generation of formation flying solar coronagraphs," in *2010 International Conference on Space Optics (ICSO)* (2010), paper 39, http://congrex.nl/icso/Papers/TPosters/39_VIVES_ICSO_PAPER.pdf.
5. G. Newkirk, Jr. and D. Bohlin, "Coronascope II: observation of the white light corona from a stratospheric balloon," in *International Astronomical Union Symposium* (1965), Vol. 23, pp. 287–291.
6. G. Newkirk, Jr. and D. Bohlin, "Reduction of scattered light in the coronagraph," Appl. Opt. **2**, 131–140 (1963).
7. B. Fort, C. Morel, and G. Spaak, "The reduction of scattered light in an external occulting disk coronagraph," Astron. Astrophys. **63**, 243–246 (1978).
8. A. V. Lenskii, "Theoretical evaluation of the efficiency of external occulting systems for coronagraphs," Sov. Astron. **25**, 366–372 (1981).
9. S. Koutchmy, "Space-borne coronagraphy," Space Sci. Rev. **47**, 95–143 (1988).
10. M. Bout, P. Lamy, A. Maucherat, C. Colin, and A. Llebaria, "Experimental study of external occulters for the Large Angle and Spectrometric Coronagraph 2: LASCO-C2," Appl. Opt. **39**, 3955–3962 (2000).
11. J. D. Purcell and M. J. Koomen, "Coronagraph with improved scattered-light properties," J. Opt. Soc. Am. **52**, 596 (1962).
12. R. Tousey, "Observations of the white light corona by rocket," Ann. d'Astrophys. **28**, 600–604 (1965).
13. A. Dollfus, "La couronne solaire vue de ballon," L'Astronomie **82**, 284 (1968).
14. J. L. Kohl, L. D. Gardner, L. Strachan, and D. M. Hassler, "Ultraviolet spectroscopy of the extended solar corona during the SPARTAN 201 mission," Space Sci. Rev. **70**, 253–261 (1994).
15. J. L. Kohl, R. Esser, L. D. Gardner, S. Habbal, P. S. Daigneau, E. F. Dennis, G. U. Nystrom, A. Panasyuk, J. C. Raymond, P. L. Smith, L. Strachan, A. A. Van Ballegooijen, G. Noci, S. Fineschi, M. Romoli, A. Ciaravella, A. Modigliani, M. C. Huber, E. Antonucci, C. Benna, S. Giordano, G. Tondello, P. Nicolosi, G. Naletto, C. Pernechele, D. Spadaro, G. Poletto, S. Livi, O. Von Der Lühe, J. Geiss, J. G. Timothy, G. Gloeckler, A. Allegra, G. Basile, R. Brusa, B. Wood, O. H. Siegmund, W. Fowler, R. Fisher, and M. Jhabvala, "The ultraviolet coronagraph spectrometer for the solar and heliospheric observatory," Sol. Phys. **162**, 313–356 (1995).
16. M. Romoli, H. Weiser, L. D. Gardner, and J. L. Kohl, "Straylight suppression in a reflecting white-light coronagraph," Appl. Opt. **32**, 3559–3569 (1993).
17. M. J. Koomen, C. R. Detwiler, G. E. Brueckner, H. W. Cooper, and R. Tousey, "White light coronagraph in OSO-7," Appl. Opt. **14**, 743–751 (1975).
18. G. E. Brueckner, R. A. Howard, M. J. Koomen, C. M. Korendyke, D. J. Michels, J. D. Moses, D. G. Socker, K. P. Dere, P. Lamy, A. Llebaria, M. Bout, R. Schwenn, G. M. Simnett, D. K. Bedford, and C. J. Eyles, "The Large Angle Spectroscopic Coronagraph (LASCO)," Sol. Phys. **162**, 357–400 (1995).
19. R. A. Howard, J. D. Moses, A. Vourlidas, J. S. Newmark, D. G. Socker, S. P. Plunkett, C. M. Korendyke, J. W. Cook, A. Hurley, J. M. Davila, W. T. Thompson, O. C. St. Cyr, E. Mentzell, K. Mehalick, J. R. Lemen, J. P. Wuelser, D. W. Duncan, T. D. Tarbell, C. J. Wolfson, A. Moore, R. A. Harrison, N. R. Waltham, J. Lang, C. J. Davis, C. J. Eyles, H. Mapson-Menard, G. M. Simnett, J. P. Halain, J. M. Defise, E. Mazy, P. Rochus, R. Mercier, M. F. Ravet, F. Delmotte, F. Auchère, J. P. Delaboudinière, V. Bothmer, W. Deutsch, D. Wang, N. Rich, S. Cooper, V. Stephens, G. Maahs, R. Baugh, D. McMullin, and T. Carter, "Sun Earth Connection Coronal and Heliospheric Investigation (SECCHI)," Space Sci. Rev. **136**, 67–115 (2008).
20. M. Romoli, E. Antonucci, S. Fineschi, D. Gardiol, L. Zangrilli, M. A. Malvezzi, E. Pace, L. Gori, F. Landini, A. Gherardi, V. Da Deppo, G. Naletto, P. Nicolosi, M. G. Pelizzo, J. D. Moses, J. Newmark, R. Howard, F. Auchère, and J. P. Delaboudinière, "The ultraviolet and visible-light coronagraph of the HERSCHEL experiment," in *Solar Wind Ten* (American Institute of Physics, 2003), Vol. 679, pp. 846–849.
21. S. Fineschi, E. Antonucci, M. Romoli, D. Gardiol, G. Naletto, S. Giordano, M. Malvezzi, V. Da Deppo, L. Zangrilli, and G. Noci, "Ultraviolet and Visible-light Coronagraphic Imager (UVCI)," Proc. SPIE **4853**, 162–171 (2003).
22. F. Auchère, M. F. Ravet-Krill, J. D. Moses, F. Rouesnel, J. P. Moalic, D. Barbet, C. Hecquet, A. Jérome, R. Mercier, J. C. Leclec'h, F. Delmotte, and J. S. Newmark, "HECOR: a HElium CORonagraphy aboard the Herschel sounding rocket," Proc. SPIE **6689**, 66890A (2007).
23. A. Thernisien, R. C. Colaninno, S. Plunkett, D. G. Socker, Q. Gong, and F. Landini, "Experimental and numerical optimization of a coronagraph external occulter. Application to SECCHI-COR2 and GOES-R SCOR," Proc. SPIE **5901**, 366–376 (2005).
24. S. Koutchmy and M. Belmahdi, "Improved measurements of scattered light level behind occulting systems," J. Opt. **18**, 265–269 (1987).
25. M. Born and E. Wolf, *Principles of Optics* (Cambridge University, 2001).
26. "Solar Probe Plus: report of the science and technology definition team," Tech. Rep. TM-2008-214161 (NASA, 2008).
27. "Solar orbiter assessment study report," Tech. Rep. SRE(2009)5 (European Space Agency, 2009).